

Orientational phase transition of microtubules in 3D using mean-field theory

Cameron Gibson^{1,2,*} Henrik Jönsson^{1,3,4,†} and Tamsin A. Spelman^{1‡}

¹ *Sainsbury Laboratory, University of Cambridge, Cambridge, UK.*

² *Department of Physics and Astronomy, Rice University, Houston, TX 77005, USA.*

³ *Department of Applied Mathematics and Theoretical Physics, University of Cambridge, Cambridge, UK.*

⁴ *Center for Environmental and Climate Research, Lund University, Lund, Sweden*

(Dated: March 6, 2023)

Microtubules are dynamic intracellular fibers, which have been observed experimentally to undergo spontaneous self-alignment. We formulate a 3D mean-field theory model to analyze the nematic phase transition of microtubules growing and interacting within a 3D space, which we compare against computational simulations. We identify a control parameter G_{eff} and predict a unique critical value $G_{\text{eff}} = 1.56$ for which a phase transition can occur. Furthermore, we show both analytically and using simulations that this predicted critical value does not depend on the presence of zippering. The mean-field theory developed here provides an analytical estimate of microtubule patterning characteristics without running time-consuming simulations and is a step towards bridging scales from microtubule behaviour to multicellular simulations.

I. INTRODUCTION

Microtubules are long filamentous fibers found in all Eukaryotic cells [1] and are vital for many processes at the cell level that are in turn essential for the survival and development of cells and the larger organism [2]. These processes include cell expansion and division [3–5]; internal transportation such as nucleus repositioning before cell division or cellulose deposition to grow cells [6–8]; fertilisation [9]; and providing mechanical structure in animal cells [2].

Microtubules form one part of the cytoskeleton (the intracellular dynamic fiber network) that also consists of actin fibres and, in animal cells, intermediate filaments [10, 11]. Microtubules continuously grow and shrink via the assembly and disassembly of the protein tubulin [12]. They undergo local stochastic behaviors such as spontaneous catastrophe, rescue, and nucleation. Microtubules interact with each other displaying behaviours via zippering predominantly at small angle interactions, induced catastrophe predominantly at large angle interactions [13, 14], and crossover severing [15]. These complex behaviors make them very interesting system to study from both a physical and mathematical perspective.

Microtubules typically nucleate from γ -tubulin complexes found on centrosomes in animal systems [16] or from the cortex in plant cells [17]. However, microtubules have also been observed nucleating in the cytoplasm of neurons [18] and the moss *physcomitrella patens* [19], demonstrating the need for a microtubule model incorporating 3D microtubule nucleation and orientation.

Microtubule networks can be viewed as analogous to the condensed matter system of nematic liquid crystals

[20, 21] as they can both be described as systems of many hard interacting rods. Furthermore, high levels of spontaneous alignment have been observed experimentally in microtubule systems which are qualitatively similar to phase transitions in nematic liquid crystals [22].

Many different computational models have been used to simulate microtubule dynamics [23–25]. CorticalSim [26, 27] is an example of an efficient event-driven model for modelling microtubules restricted to a plane. It has been used to show, for example, that the co-alignment of microtubules nucleating from parent microtubules supports whole network alignment [28]. A different example model named Cytosim [29] is a 3D force-based microtubule model used, for example, to consider how molecular motor patterns can direct filament directions [30]. A third model example called Tubulaton [31, 32] is a 3D rule-based model used, for example, to study the importance of the crossover-severing protein katanin to microtubule ordering in plant protoplasts, as observed in experiments [33].

Similarly, several mathematical models have been proposed to analyse cytoskeletal dynamics [34–37]. One useful continuum theory approach is mean-field theory, which is used extensively to model condensed matter systems [38]. Mean-field theory in the context of cytoskeletal dynamics was introduced by Dogterom and Leibler [39]. They derived governing differential equations which incorporated the fundamental microtubule properties of growing, shrinking, catastrophe and rescue. This model was later expanded to include more complex microtubule behaviours [39–44]. This was extended to the first 2D mean-field theory model [43], with subsequent models introducing more complex microtubules behaviours such as induced catastrophes [44], where they showed the existence of a phase transition under certain assumptions.

There is only one extension of mean-field to 3D the authors are aware of [45], and this model is restricted to the specific case of microtubules only nucleating radially

* cameron.gibson@rice.edu

† henrik.jonsson@slcu.cam.ac.uk

‡ tamsin.spelman@slcu.cam.ac.uk

from a prescribed central centrosome within a bounded domain, with the model including interaction dynamics between microtubules and the cell boundary but not between microtubules themselves. In this paper, the 2D mean-field model of [44] is extended to 3D in a novel way incorporating microtubule interaction dynamics in the different setup of microtubules nucleating randomly within a 3D domain. The differences and similarities between 2D and 3D are then highlighted and the theoretical predictions of the 3D model are compared to results obtained from 3D simulations from Tubulaton [31].

This paper is organized as follows. The models are outlined in Sec. II. Specifically in Sec. II A, the 3D mean field model is derived and in Sec. II B, the computational model Tubulaton used to validate the mean-field model is described. The results are presented in Sec. III. In Sec. III A, the constraints on the system that allow for a phase transition in 3D are determined. In Sec. III B, we compare our 3D mean-field model with the previous 2D mean-field theory model [44]. Finally, the predictions of the mean-field theory model are compared to the results of the computational simulations in Sec. III C, with the effects of severing considered in Sec. III D, and to experimental values from the literature in Sec. III E before concluding in Sec. IV.

II. MODELS

Here, the 3D mean-field mathematical model is formulated and the computational model is briefly outlined. Throughout this paper, spherical polar coordinates are used to describe directions in 3D space, with (θ, ϕ) representing polar and azimuthal angles, respectively.

A. Mean-Field Theory

Each microtubule is modelled as a series of segments. It is assumed that unhindered microtubules grow in a straight line, but can change direction with a prescribed angle-dependent probability when two microtubules collide. When the microtubule changes direction, the old segment becomes static (neither growing nor shrinking) and a new segment starts growing in the new direction, anchored to the previous segment. The microtubules grow (and shrink) in segments, with joints allowing each segment to be oriented in a different direction.

It is assumed that that microtubules isotropically nucleate everywhere in 3D space at a constant rate r_n , initiating in a growing state with static minus end and growing plus end. Microtubules are always static at the minus end, and are either growing or shrinking at the plus end with speed v^+ or v^- , respectively. The plus end changes from shrinking to growing via spontaneous rescue with rate r_r and changes from growing to shrinking via spontaneous catastrophe with rate r_c .

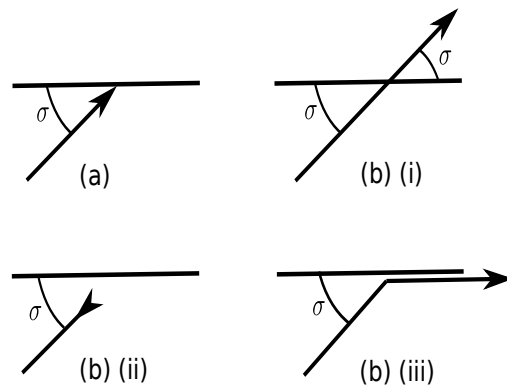


FIG. 1: Illustration of different microtubule interactions. These behaviours are included in both the mean-field model and the simulations. (a) Initial collision where the growing microtubule segment collides with another microtubule at angle σ . (b) Different responses to the collision (i) Crossover: the growing segment continues to grow unhindered. (ii) Induced catastrophe: the segment switches from growing to shrinking. (iii) Zippering: the segment starts to grow parallel to the segment with which it collides.

When a growing segment collides with another microtubule, either there is an induced catastrophe (it starts shrinking), crossover (it keeps growing unhindered) or zippering (it starts growing parallel to the second segment) with respective probabilities $P_c(\sigma)$, $P_x(\sigma)$ and $P_z(\sigma)$ all written as functions of the collision angle σ (Fig. 1).

1. Master Equations

In this subsection, the governing 3D mean-field differential equations will be derived, following a similar argument to that outlined in detail for a 2D framework [44].

The density of microtubules is assumed to be large enough for this discrete system to be accurately approximated by continuous variables. Therefore $m_i^{+/-/0}(l, \theta, \phi, t)$ is defined as the density of microtubule segments in direction (θ, ϕ) of length l at time t with $+/-/0$ indicating a growing/shrinking/inactive segment, respectively, and i indexing the segments (letting $i = 1$ index the segment that has nucleated).

Then, the master equations governing the evolution of the system can be expressed in terms of flux terms de-

noted Φ_{event} as

$$\begin{aligned}\partial_t m_i^+(l, \theta, \phi, t) &= \Phi_{\text{growth}} + \Phi_{\text{rescue}} - \Phi_{\text{spontcat}} \\ &\quad - \Phi_{\text{inducedcat}} - \Phi_{\text{zipper}}, \\ \partial_t m_i^-(l, \theta, \phi, t) &= \Phi_{\text{shrinkage}} - \Phi_{\text{rescue}} + \Phi_{\text{spontcat}} \\ &\quad + \Phi_{\text{inducedcat}} + \Phi_{\text{reactivation}}, \\ \partial_t m_i^0(l, \theta, \phi, t) &= \Phi_{\text{zipper}} - \Phi_{\text{reactivation}},\end{aligned}\quad (1)$$

where ∂_x denotes partial differentiation with respect to x . Explicit expressions for the fluxes corresponding to behaviours independent of microtubule interactions follow from physical definitions as

$$\begin{aligned}\Phi_{\text{growth}} &\equiv (\partial_t l) \partial_l m_i^+ = -v^+ \partial_l m_i^+(l, \theta, \phi, t), \\ \Phi_{\text{shrinkage}} &\equiv (\partial_t l) \partial_l m_i^- = v^- \partial_l m_i^-(l, \theta, \phi, t), \\ \Phi_{\text{rescue}} &\equiv r_r m_i^-(l, \theta, \phi, t), \\ \Phi_{\text{spontcat}} &\equiv r_c m_i^+(l, \theta, \phi, t).\end{aligned}\quad (2)$$

Flux terms associated with microtubule interactions have more complex formulations. The reactivation flux can be written as

$$\begin{aligned}\Phi_{\text{reactivation}} &\equiv v^- \int d\theta' \int d\phi' \sin(\theta') \\ &\quad \times m_{i+1}^-(l' = 0, \theta', \phi', t) p_{\text{unzip}}(\theta, \phi, l | \theta', \phi', t),\end{aligned}\quad (3)$$

where $p_{\text{unzip}}(\theta, \phi, l | \theta', \phi', t)$ is the probability that the $(i+1)^{\text{th}}$ segment shrinks from the direction (θ', ϕ') to length $l' = 0$ at time t and reactivates the i^{th} segment of length l in direction (θ, ϕ) . Detailed arguments as to why p_{unzip} does not contribute in the steady state case can be found in [44], which naturally extend from 2D to 3D.

The length density of microtubules pointing in direction (θ, ϕ) is

$$\begin{aligned}k(\theta, \phi, t) &\equiv \sum_{i=1}^{\infty} \int dl [m_i^+(l, \theta, \phi, t) + m_i^-(l, \theta, \phi, t) \\ &\quad + m_i^0(l, \theta, \phi, t)] l.\end{aligned}\quad (4)$$

The diameter of the microtubules is defined as d_m . The induced catastrophe flux term is given by

$$\begin{aligned}\Phi_{\text{inducedcat}} &\equiv d_m v^+ m_i^+(l, \theta, \phi, t) \int d\theta' \int d\phi' \sin(\theta') \\ &\quad \times c(\theta, \theta', \phi - \phi') k(\theta', \phi', t),\end{aligned}\quad (5)$$

where it is defined that

$$c(\theta, \theta', \phi - \phi') \equiv |\sin(\sigma)| P_c(\sigma(\theta, \theta', \phi - \phi')), \quad (6)$$

and the angle between the two directions (θ, ϕ) and (θ', ϕ') is written as

$$\sigma \equiv \arccos(\sin(\theta) \sin(\theta') \cos(\phi - \phi') + \cos(\theta) \cos(\theta')). \quad (7)$$

This flux term represents the rate at which a microtubule of length l growing in direction (θ, ϕ) collides with an obstructing microtubule oriented in any direction. A significant difference from the 2D case is the factor of d_m

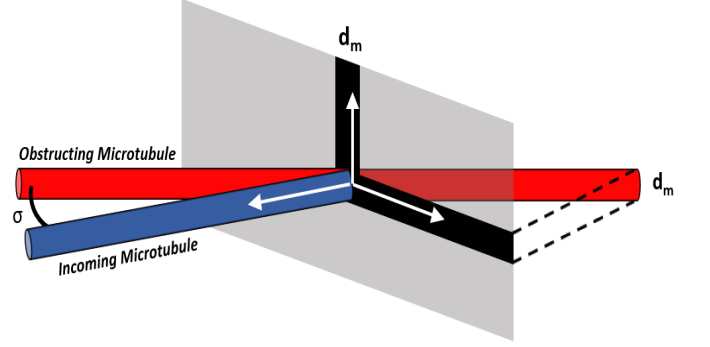


FIG. 2: A graphical representation of Eq. 5. A second microtubule obstructs an incoming microtubule at an angle of σ . When the obstructing microtubule is projected onto the plane orthogonal to the incoming microtubule, we consider collisions as occurring in a length of the microtubule diameter d_m in the direction orthogonal to both microtubules.

in Eq. 5. In 2D, two thin infinite lines will always collide if they are not parallel. However, in 3D, two thin non-parallel rods can pass over each other without colliding. This difference in the 3D case can be addressed by considering two microtubules to collide when they are within a distance of the microtubule diameter d_m of each other. This is represented graphically in Fig. 2 and explained as follows. The $|\sin(\sigma)|$ factor in Eq. 6 projects the length density $k(\theta', \phi')$ to a plane perpendicular to the direction (θ, ϕ) of an incoming microtubule. The microtubule diameter d_m is included as a distance in the direction perpendicular to both microtubules below which two microtubules interact. The need for a factor of d_m in the flux term can also be explained on dimensional grounds since it ensures that both sides of Eq. 5 have the same dimensionality ($\text{Length}^{-4} \times \text{Time}^{-1}$).

The flux term Φ_{zipper} is defined similarly to $\Phi_{\text{inducedcat}}$ in Eq. 5 but with c replaced by z (each of which has a factor of P_c and P_z , respectively).

2. Control Parameter

An important parameter of the system is $g = r_r/v^- - r_c/v^+$ [43, 44]. Physically, g corresponds to the non-interacting behavior of the microtubules. The limit $g \rightarrow -\infty$ corresponds to the average length of the microtubules tending to zero resulting in an isotropic system, whilst $g \rightarrow \infty$ corresponds to the average length of the microtubules tending to infinity resulting in a completely ordered (anisotropic) system. Following the earlier analogy to a phase transition in a liquid crystal system, this control parameter g is analogous to temperature in liquid crystals [20, 21]. Therefore, it is expected that there will be an orientational phase transition as g increases from

negative infinity, which has been shown to occur perturbatively in 2D [44]. Importantly, it is noted that the only physically realizable values of g are negative, since positive g corresponds to unbounded growth.

3. Steady State System

Here, the previously derived master equations (Eq. 1) are reduced to the steady state case. The arguments are similar to the 2D derivation [44].

Firstly, for simplification it is noted expressions like Eq. 5 can be summarized by defining the dimensionless linear operator

$$F[h](\theta, \phi) \equiv \alpha \int_0^\pi d\theta' \int_0^{2\pi} d\phi' \sin(\theta') f(\sigma(\theta, \theta', \phi - \phi')) h(\theta', \phi'), \quad (8)$$

for $F \in [C, Z]$ and h any function of (θ, ϕ) .

Other quantities useful for expressing the steady state will now be defined. The average segment length $l(\theta, \phi)$ in the direction (θ, ϕ) is defined as

$$\frac{1}{l(\theta, \phi)} = -g + d_m \int d\theta' \int d\phi' \sin(\theta') [c(\theta, \theta', \phi - \phi') + z(\theta, \theta', \phi - \phi')] k(\theta', \phi'). \quad (9)$$

The ratio of inactive (static at both ends) to active (both growing and shrinking) segments $Q(\theta, \phi)$ in the direction (θ, ϕ) is defined as

$$Q(\theta, \phi) = \frac{m^0(\theta, \phi)}{m^+(\theta, \phi) + m^-(\theta, \phi)}. \quad (10)$$

Using $v^+ m_i^+ = v^- m_i^-$ in the steady state system with bounded growth, the density of active segments $r(\theta, \phi)$ in the direction (θ, ϕ) is defined as

$$r(\theta, \phi) = \left(1 + \frac{v^+}{v^-}\right) l(\theta, \phi) \sum_{i=1}^{\infty} m_i^+(\theta, \phi). \quad (11)$$

To formulate non-dimensional steady state equations, a variable l_0 is defined with dimensions of length

$$l_0 = \left[\left(\frac{1}{v^+} + \frac{1}{v^-} \right) \frac{r_n}{4\pi} \right]^{-\frac{1}{4}}, \quad (12)$$

which is used to non-dimensionalize parameters and variables. Note that r_n is normalized by 4π (obtained by integrating the differential solid angle $\sin(\theta)d\theta d\phi$ over the entire sphere) in 3D, in contrast with normalizing by 2π in 2D. The dimensionless length ratio α , defined by

$$\alpha \equiv d_m/l_0, \quad (13)$$

will be a common quantity used to simplify the equations. The dimensionless quantities are then $G = gl_0$, $L = ll_0^{-1}$, $K = kl_0^2$ and $R = rl_0^3$.

The control parameter for this system is therefore the non-dimensional form of g which is explicitly

$$G = \left[\frac{4\pi v^+ v^-}{r_n (v^+ + v^-)} \right]^{\frac{1}{4}} \left(\frac{r_r}{v^-} - \frac{r_c}{v^+} \right). \quad (14)$$

Using these simplifications and the non-dimensional variables, the steady state equations can be written as

$$\frac{1}{L(\theta, \phi)} = -G + C[K](\theta, \phi) + Z[K](\theta, \phi), \quad (15a)$$

$$K(\theta, \phi) = L(\theta, \phi)(1 + Q(\theta, \phi))R(\theta, \phi), \quad (15b)$$

$$Q(\theta, \phi) = Z[LK(1 + Q)](\theta, \phi), \quad (15c)$$

$$R(\theta, \phi) = L(\theta, \phi) + L(\theta, \phi)K(\theta, \phi)Z[R](\theta, \phi). \quad (15d)$$

There is a symmetry in Eqs. 15 under $l_0 \rightarrow -l_0$ (where $\alpha \rightarrow -\alpha$ under this transformation). This arises as Eq. 12 has a positive and negative root. Since l_0 can be either positive or negative and $g < 0$ for a physically realizable system, any nonzero real G describes a physically realizable system.

4. Isotropic Solution

Next, the solution of the steady state equations just derived Eq. 15 will be calculated in the isotropic case.

The calculation will require the spherical harmonics [46, 47]. These are a complete set of orthogonal functions defined on the surface of a sphere with two indices (ℓ and m), which can be defined by the real-valued functions

$$Y_\ell^m(\theta, \phi) = \begin{cases} (-1)^{m+1} \sqrt{\frac{2\ell+1}{2\pi} \frac{(\ell-|m|)!}{(\ell+|m|)!}} P_\ell^{-m}(\cos(\theta)) \sin(m\phi) & m < 0, \\ \sqrt{\frac{2\ell+1}{4\pi}} P_\ell^0(\cos(\theta)) & m = 0, \\ (-1)^m \sqrt{\frac{2\ell+1}{2\pi} \frac{(\ell-m)!}{(\ell+m)!}} P_\ell^m(\cos(\theta)) \cos(m\phi) & m > 0. \end{cases} \quad (16)$$

Here, P_ℓ^m are the associated Legendre polynomials, defined in terms of the standard Legendre polynomials P_ℓ as

$$P_\ell^m(\cos \theta) = (-1)^m (\sin \theta)^m \frac{d^m}{d(\cos \theta)^m} (P_\ell(\cos \theta)), \quad (17)$$

where

$$P_\ell(x) = \frac{1}{2^\ell \ell!} \frac{d^\ell}{dx^\ell} (x^2 - 1)^\ell. \quad (18)$$

The spherical harmonics defined by Eq. 16 provide an orthonormal basis of eigenfunctions of the linear operator

defined in Eq. 8, with the eigenvalue equation

$$F[Y_\ell^m(\theta, \phi)] = \frac{4\pi\alpha\mathfrak{F}_\ell}{(2\ell+1)} Y_\ell^m(\theta, \phi), \quad (19)$$

where a functional redefinition of the form $\mathfrak{F}(\cos(\sigma)) \equiv f(\sigma)$ has been introduced, where $f \in [c, z]$ (defined in Eq. 6) and $\mathfrak{F} \in [\mathfrak{C}, \mathfrak{Z}]$, respectively, and with σ already defined in Eq. 7.

To prove Eq. 19, first note that the Legendre polynomials $P_\ell(x)$ defined in Eq. 18 form a complete set of orthogonal functions $P_\ell(x) : \mathbb{R} \rightarrow \mathbb{R}$, and a (unique) Legendre expansion is given by

$$\mathfrak{F}(\cos(\sigma)) = \sum_{\ell=0}^{\infty} \mathfrak{F}_\ell P_\ell(\cos(\sigma)), \quad (20)$$

$$\text{where } \mathfrak{F}_\ell = \frac{2\ell+1}{2} \int_{-1}^1 \mathfrak{F}(x) P_\ell(x) dx. \quad (21)$$

Then, the spherical harmonic addition theorem [46, 47]

$$P_\ell(\cos(\sigma)) = \frac{4\pi}{2\ell+1} \sum_{m=-\ell}^{\ell} Y_\ell^m(\theta, \phi) Y_\ell^{\dagger m}(\theta', \phi'), \quad (22)$$

where \dagger denotes complex conjugation, can be used to rewrite Eq. 20 as

$$f(\sigma) = \sum_{\ell=0}^{\infty} \frac{4\pi}{2\ell+1} \sum_{m=-\ell}^{\ell} \mathfrak{F}_\ell Y_\ell^m(\theta, \phi) Y_\ell^{\dagger m}(\theta', \phi'). \quad (23)$$

Substituting this expression for $f(\sigma)$ into Eq. 8 with the spherical harmonic Y_ℓ^m as the argument of F gives

$$F[Y_\ell^m(\theta, \phi)] = \alpha \int_0^\pi d\theta' \int_0^{2\pi} d\phi' \sin(\theta') \sum_{n=0}^{\infty} \sum_{p=-n}^n \frac{4\pi\mathfrak{F}_n}{2n+1} Y_n^p(\theta, \phi) Y_n^{\dagger p}(\theta', \phi') Y_\ell^m(\theta', \phi'). \quad (24)$$

Using the standard orthogonality relation of spherical harmonics

$$\int_0^\pi d\theta' \int_0^{2\pi} d\phi' \sin(\theta') Y_\ell^m(\theta', \phi') Y_{\ell'}^{m'}(\theta', \phi') = \delta_{\ell\ell'} \delta_{mm'}, \quad (25)$$

where the Kronecker delta δ_{ab} takes the value 1 iff $a \equiv b$ and 0 otherwise. This allows Eq. 24 to be simplified to

$$F[Y_\ell^m(\theta, \phi)] = \sum_{n=0}^{\infty} \sum_{p=-n}^n \frac{4\pi\alpha\mathfrak{F}_n}{2n+1} Y_n^p(\theta, \phi) \delta_{n\ell} \delta_{pm}, \quad (26)$$

which is equivalent to Eq. 19.

Using this, the isotropic solution can be now be calculated. In the isotropic (and stationary) state of the system, which will be denoted by overbars, all angular dependence drops out and Eqs. 15 becomes

$$\frac{1}{\bar{L}} = -G + 4\pi\alpha(\mathfrak{C}_0 + \mathfrak{Z}_0)\bar{K} \quad (27a)$$

$$\bar{K} = \bar{L}(1 + \bar{Q})\bar{R} \quad (27b)$$

$$\bar{Q} = 4\pi\alpha\mathfrak{Z}_0\bar{L}\bar{K}(1 + \bar{Q}) \quad (27c)$$

$$\bar{R} = \bar{L} + 4\pi\alpha\mathfrak{Z}_0\bar{L}\bar{K}\bar{R}. \quad (27d)$$

where the identity $F[1] = 4\pi\alpha\mathfrak{F}_0$ was used, which arises from setting $\ell = m = 0$ in Eq. 19.

Substituting and rearranging Eqs. 27 reduces to the expression

$$\bar{K}(4\pi\alpha\mathfrak{C}_0\bar{K} - G)^2 = 1, \quad (28)$$

with the details outlined in Appendix. A. The quantity \bar{K} is always positive. \mathfrak{C}_0 is also taken to be positive and it will be shown in Sec. III B that this agrees well with experimental values. If $\alpha < 0$ and $G > 0$, then Eq. 28 gives an expression for G in terms of \bar{K} as

$$G = 4\pi\alpha\mathfrak{C}_0\bar{K} + \bar{K}^{-\frac{1}{2}}. \quad (29)$$

For given values of $\alpha < 0$ and \mathfrak{C}_0 , there is clearly a uniquely determined value of G for each value of \bar{K} . The converse is true since the right hand side of Eq. 29 is a strictly decreasing function of positive \bar{K} which tends to ∞ for $\bar{K} \rightarrow 0$ and tends to $-\infty$ for $\bar{K} \rightarrow \infty$. Furthermore, $G > 0$ gives us the constraint $\bar{K} < |4\pi\alpha\mathfrak{C}_0|^{-2/3}$ (the value of \bar{K} for which $G = 0$).

An identical argument for $G < 0$, $\alpha > 0$ leads to the same conclusions, giving the general constraint that holds in both cases ($\alpha < 0$, $G > 0$) and ($\alpha > 0$, $G < 0$) of

$$0 < \bar{K} < |4\pi\alpha\mathfrak{C}_0|^{-\frac{2}{3}}. \quad (30)$$

Therefore, there is a density limit to the system above which it is not possible to have an isotropic system. This density limit decreases with increasing d_m (which is equivalent to increasing $|\alpha|$). This makes sense physically since greater d_m increases interaction between segments, therefore preventing an isotropic solution at lower density systems.

Additionally, as it will be needed in Sec. III B, note that Eqs. 27 also lead to the expression

$$G = \frac{4\pi\alpha(\mathfrak{C}_0 + \mathfrak{Z}_0)\bar{N} - 1}{\bar{N}^{\frac{1}{3}}(4\pi\alpha\mathfrak{Z}_0\bar{N} - 1)^{\frac{2}{3}}}, \quad (31)$$

with the detailed derivation outlined in Appendix A.

B. Simulation

The predictions from the 3D mean-field theory mathematical model just derived will later be validated against 3D microtubule simulations using Tubulaton, which will be briefly explained here. Tubulaton uses a discretized model of microtubule dynamics modeling each microtubule individually as a line of end-to-end unit vectors, each corresponding to 8nm and representing a single ring

of tubulin. Microtubules grow and shrink by adding or removing unit vectors at their ends. Microtubule interaction dynamics such as zippering and induced catastrophe (Fig. 1) are incorporated, as well as individual microtubule dynamic behaviors such as nucleation and spontaneous catastrophe. An external membrane is prescribed within which microtubules remain. Previous papers contained a detailed description of Tubulaton [32, 33], so here we will focus on specific changes and additions that have been made with the purpose of comparing to the mean-field theory model.

To reflect mean-field theory defined within an infinite volume without a boundary, we construct three spheres of decreasing radii all centred on the same point. This setup was chosen instead of periodic boundary conditions due to complications arising from how microtubules would interact with each other at the boundary. The largest sphere forms the external boundary of the system, the middle sphere defines the region where microtubules nucleate, and the smallest sphere region within which we calculate the level of anisotropy.

Tubulaton was extended to improve the originally encoded assumption that the probability of induced catastrophe and zippering are fixed. Instead, they were varied as a function of collision angle. This reflects experimental observations [13] and the mean-field assumptions. For our simulations including the effects of zippering we match experimental observations [13] by taking the function described later by Fig. 4, or we set it equal to zero remove the effects of zippering.

The ability to vary r_c and r_n was already incorporated in Tubulaton. Effects of spontaneous rescue are not included but these are unnecessary since the regime of interest is negative g (whereas G can be either positive or negative) and varying r_c gives the full range of negative values of g , which is still true when we take $v^+ = v^-$ in all our simulations. However, the region of $r_c - r_n$ within which we performed simulations was restricted by convergence and computational time. At low r_c , we observed very large fluctuations in segment density for small changes in r_n . On the other hand, at large r_c , we observed that the value of r_n required for a steady state density grew sharply leading to long computational times.

Details of the parameter values used in the simulations are included in Appendix. D and shown in Table. A2. Within the limit of 10,000 time steps (15-30 min simulated time), the density of microtubule segments number converged (see Fig. A1) so simulations are expected to have reached a steady state as was assumed in the mean-field theory analysis. When comparing r_n with r_c for constant segment density, larger default sphere radii are used but otherwise the smaller default sphere radii are used as they are less computationally expensive. A snapshot of a Tubulaton simulation is illustrated in Fig. 3.

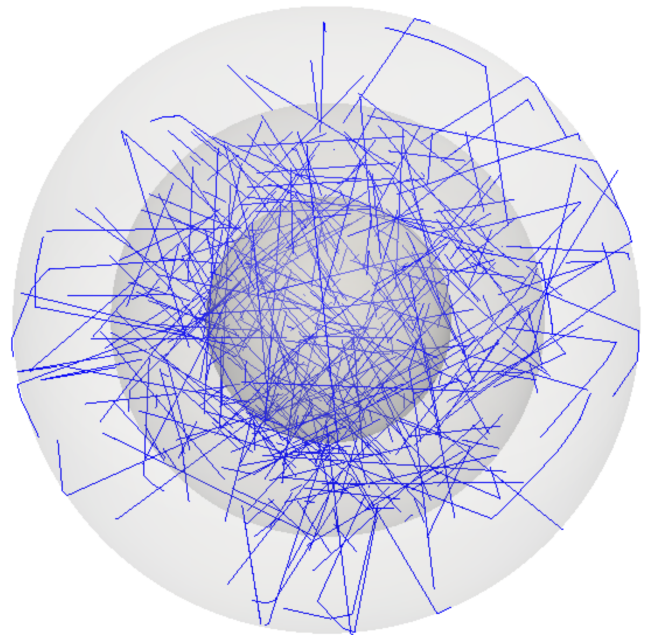


FIG. 3: Snapshot of a Tubulaton simulation showing all the microtubules within the external membrane. The three transparent spheres represent the external membrane, nucleation region and analysis region in descending size of radius.

C. Order Parameter

Following earlier comparisons to nematic liquid crystals, the standard nematic order parameter [20, 21, 48] is used to quantify the alignment of the microtubules in the system. In D dimensions, this is a unique tensor up to an overall factor, which is normalized by setting it equal to unity in the completely anisotropic state. It is defined as

$$S_{ab} = \left\langle \frac{D}{D-1} n_a n_b - \frac{1}{D-1} \delta_{ab} \right\rangle, \quad (32)$$

where $\langle \rangle$ denotes taking a weighted average over every microtubule segment, each of which is parameterized by the D -dimensional unit vector n and weighted by the segment length. Performing this averaging using an integral weighted by the microtubule length density in each direction (with $D = 3$), gives the 3x3 matrix with components (with $i, j = 1, 2, 3$).

$$S_{ij} = \frac{\int_0^\pi d\theta \int_0^{2\pi} d\phi \sin(\theta) K(\theta, \phi) \left(\frac{3}{2} n \otimes n - \frac{1}{2} \mathcal{I} \right)_{ij}}{\int_0^\pi d\theta \int_0^{2\pi} d\phi \sin(\theta) K(\theta, \phi)}. \quad (33)$$

For calculating the order parameter S in simulations, the discretized form of Eq. 33 is used

$$S = \frac{\sum_\mu \left(\frac{3}{2} n^\mu \otimes n^\mu - \frac{1}{2} \mathcal{I} \right)_{ij}}{\sum_\mu 1}, \quad (34)$$

where μ labels each microtubule segment, each of which is associated to a unit direction vector n^μ .

This matrix with components S_{ij} has three eigenvalues which are all zero if and only if the system is in its completely isotropic state. We define S as the maximal absolute value of the eigenvalue of this matrix. A larger value of S indicates a higher level of anisotropy so an increasing S indicates that a system is changing from an isotropic state to an anisotropic state [49].

D. Visualisation and code availability

All numerical work and graphing in Sec. III was performed using MATLAB R2021a. Simulations were visualized using Paraview 5.0.1. All scripts used for plotting and running Tubulaton simulations are available in the software repository at https://gitlab.com/slucu/team/HJ/publications/gibson_et_al_2022.

III. RESULTS

A. Conditions for a Phase Transition

Here, we will consider which values of microtubule properties allow for a change from disorder to order as g is increased in order to determine the conditions for a phase transition to occur. Assuming that the change in order is continuous, when the order parameter becomes small and non-zero, the steady-state solution will be a small perturbation from the isotropic solution. Therefore, we will perturb the isotropic solution from Sec. II A 4 and determine what conditions allow a solution to exist with small order parameter. The perturbative solution is derived in Appendix. B and results in the eigenvalue equation

$$(1 - 4\pi\alpha\bar{\mathfrak{J}}_0\bar{N})\kappa(\theta, \phi) = -2\bar{N}C[\kappa(\theta, \phi)], \quad (35)$$

where $\bar{N} = \bar{L}\bar{K}$ and $K = \bar{K}(1 + \kappa)$ defines the first order perturbation $\kappa(\theta, \phi)$. This eigenvalue equation is a special case of Eq. 19 so the spherical harmonics defined in Eq. 16 form an orthonormal basis of eigenfunctions. Since the eigenvalues in Eq. 19 depend only on the lower index ℓ of the spherical harmonics, each ℓ determines a different value of \bar{N} , denoted \bar{N}_ℓ^* given explicitly by

$$\bar{N}_\ell^* = \left(4\pi\alpha\bar{\mathfrak{J}}_0 - \frac{8\pi\alpha}{2\ell+1}\mathfrak{C}_\ell\right)^{-1}, \quad (36)$$

for which there is a potential phase transition. Directly substituting these values of \bar{N} into Eq. 31 gives us the corresponding values of G as

$$G_\ell^* = \left[1 + \frac{(2\ell+1)\mathfrak{C}_0}{2\mathfrak{C}_\ell}\right] \left[-\frac{8\pi\alpha\mathfrak{C}_\ell}{2\ell+1}\right]^{\frac{1}{3}}, \quad (37)$$

which are by extension also indexed by ℓ .

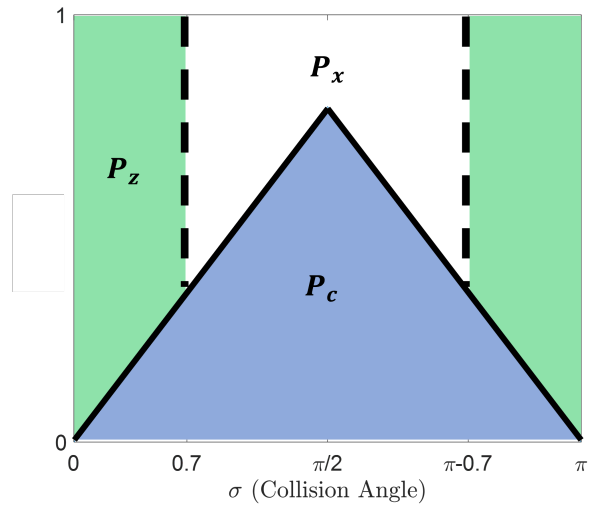


FIG. 4: Probability of induced catastrophe (P_c), induced zippering (P_z) and crossover ($P_x = 1 - P_c - P_z$) as a function of collision angle σ used in our analytical calculation and computational simulations reflecting experimental observations. The point of maximum P_c is at $(\pi/2, \pi/4)$.

The location of the possible phase transition depends only on the catastrophe probability function and is independent of the zippering probability function, since there is no dependence on $\bar{\mathfrak{J}}_\ell$ in Eq. 37. This is similar to the 2D case [44].

In order to explicitly evaluate Eq. 37, we approximate experimental observations that catastrophe probability increases approximately linearly as a function of collision angle to around 0.7 at $\pi/2$ collision angle [13]. $P_c(\sigma)$ is therefore chosen to be two concatenated linear functions through the three points $(0, 0)$, $(\frac{\pi}{2}, \frac{\pi}{4})$, and $(\pi, 0)$. Zippering probability is similarly approximated, with zippering occurring primarily at lower angles, by taking $P_z(\sigma) = 1 - P_c(\sigma) \forall \sigma \leq 0.7, \sigma \geq \pi - 0.7$ and $P_z(\sigma) = 0$ otherwise (Fig. 4).

Quantities required to explicitly calculate the possible phase transition location can now be numerically calculated. In particular,

$$\mathfrak{C}_\ell = \frac{2\ell+1}{2} \int_0^\pi \sin^2(y) P_c(y) P_\ell(\cos(y)) dy, \quad (38)$$

an expression obtained from Eq. 21 through the change of variables $x \equiv \cos(y)$. Splitting the integral's domain in half, making a change of variables in $[0, \pi/2]$ by $y \rightarrow (\pi - y)$ and using the identity $P_\ell(-x) = (-1)^\ell P_\ell(x)$, results in

$$\mathfrak{C}_\ell = \frac{(1 + (-1)^\ell)(2\ell+1)}{2} \int_0^{\frac{\pi}{2}} \frac{1}{2} y \sin^2(y) P_\ell(\cos(y)) dy. \quad (39)$$

The Legendre coefficients \mathfrak{C}_ℓ are fundamental to evaluating the control parameter and identifying the location of

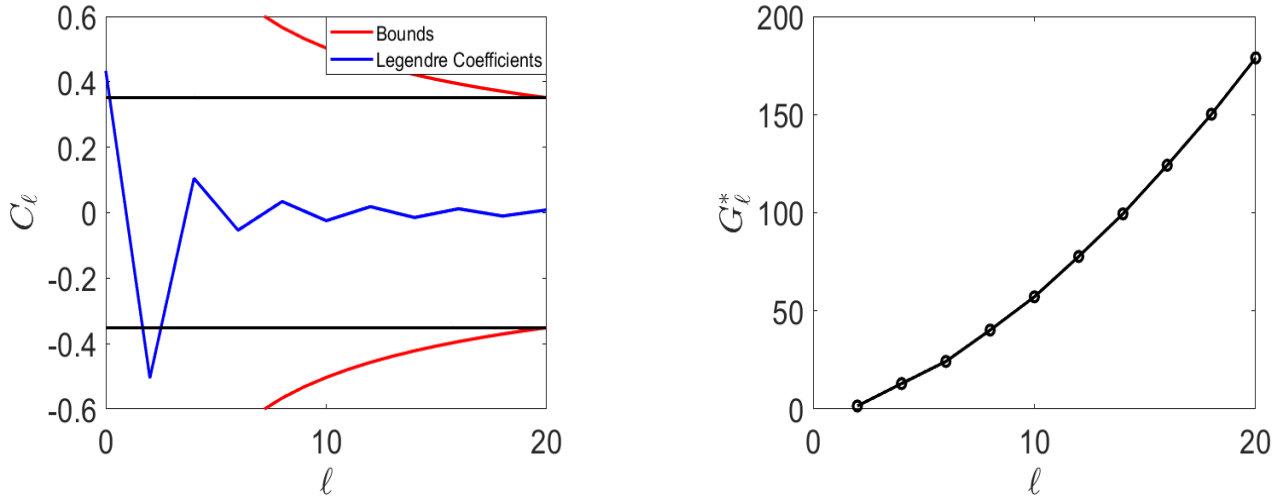


FIG. 5: Effect of varying the Legendre coefficient index ℓ (for even values of ℓ between 0 and 20) of the spherical harmonic perturbation $\kappa = Y_\ell^m$ (normalized as in Eq. 16) on (a) Legendre coefficients \mathfrak{C}_ℓ as defined in Eq. 38 and (b) corresponding control parameter values G_ℓ^* . In (a) the red line shows the analytical upper and lower bounds of the Legendre coefficients while the green horizontal lines are equal to the size of these bounds at $\ell = 20$ and is included for comparison.

a potential phase transition. \mathfrak{C}_ℓ identically vanishes for all odd ℓ . The magnitudes for even ℓ up to $\ell = 20$ are plotted in Fig. 5a, which decrease in this range. Note that $\mathfrak{C}_0 = 0.43$ (2sf) provides a positive value for \mathfrak{C}_0 which was previously asserted as reasonable for Eq. 28. As shown in [50] using an improved Bernstein inequality [51, 52], there is a general bound on Legendre coefficients

$$|\mathfrak{C}_\ell| \leq \frac{2}{\sqrt{\pi(2\ell-1)}} \int_{-1}^1 \frac{|\mathfrak{C}'(x)|}{(1-x^2)^{\frac{1}{4}}} dx, \quad (40)$$

which is plotted on Fig. 5a. Since the magnitude of the bound is decreasing, the bound at $\ell = 20$ shows that \mathfrak{C}_2 must be the largest Legendre coefficient.

The value of the control parameter G_ℓ^* corresponding to each Legendre coefficient is shown in Fig. 5b. The value of G_ℓ^* (Eq. 37) increase for even values of ℓ up to $\ell = 20$. Since all values of G_ℓ^* are positive, l_0 can be taken to be negative so that $g = G/l_0$ is negative since we only wish to consider physically realizable solutions with bounded growth (as discussed in Sec. II A 2). However, no particular value of G_ℓ^* has been singled out to correspond to a phase transition. To do this, it is necessary to consider which perturbations (ℓ) leads to a change in the order parameter defined in Eq. 33.

The perturbed order parameter can be calculated. Perturbing away from the isotropic case $K = \bar{K}$, where the order parameter is zero, the new variable $K \equiv \bar{K} \left(1 + \sum_{\ell,m} \beta_\ell^m Y_\ell^m\right)$ is defined, where β are taken to be small constants. Expanding Eq. 33 to first order in β ,

the order parameter for the perturbed system is

$$S_\beta = \sum_{\ell=0}^{\infty} \sum_{m=-\ell}^{\ell} \beta_\ell^m \frac{\int_0^\pi d\theta \int_0^{2\pi} d\phi \sin(\theta) Y_\ell^m(\frac{3}{2}n \otimes n - \frac{1}{2}\mathcal{I})}{\int_0^\pi d\theta \int_0^{2\pi} d\phi \sin(\theta)}. \quad (41)$$

The tensor components $Q_{ij} \equiv (\frac{3}{2}n \otimes n - \frac{1}{2}\mathcal{I})_{ij}$ from Eq. 32 can be written in terms of only $\ell = 2$ spherical harmonics as

$$\begin{aligned} Q_{11} &= \sqrt{\frac{3\pi}{10}} (Y_2^{-2} + Y_2^2) - \sqrt{\frac{\pi}{5}} Y_2^0, \\ Q_{22} &= -\sqrt{\frac{3\pi}{10}} (Y_2^{-2} + Y_2^2) - \sqrt{\frac{\pi}{5}} Y_2^0, \\ Q_{33} &= \sqrt{\frac{4\pi}{5}} Y_2^0, \\ Q_{12} &= \sqrt{\frac{-3\pi}{10}} (Y_2^{-2} - Y_2^2), \\ Q_{13} &= \sqrt{\frac{3\pi}{10}} (Y_2^{-1} - Y_2^1), \\ Q_{23} &= \sqrt{\frac{-3\pi}{10}} (Y_2^{-1} + Y_2^1). \end{aligned} \quad (42)$$

Due to the spherical harmonic orthogonality condition of Eq. 25, the only nonzero contribution to Eq. 41 is from β_2^m for $m = -2, -1, 0, 1, 2$. This claim was verified numerically by calculating the eigenvalues of the order parameter for perturbations $\kappa = \beta Y_\ell^m$ for $\ell = 1, \dots, 200$ (testing each of $m = -2\ell, \dots, 2\ell$ in turn) for $\beta = 1$ and $\beta = 1/100$. All $\ell \neq 2$ perturbations led to zero eigenvalues. The eigenvalues of the order parameter S were $(0.77, -0.77, 0)$ for $\kappa = Y_2^m$ for $m = -2, -1, 1, 2$ and

(-0.06, -0.06, 0.13) for $m = 0$. This confirms that only the $\ell = 2$ spherical harmonic perturbation causes disorder in the system and taking $\beta = 1$ is small enough to justify using a perturbative analysis.

Therefore, setting $l = 2$ in Eq. 37, this mean-field theory model can only exhibit a phase transition at $G^* \equiv G_2^* = 1.56\alpha^{1/3}$.

B. Comparison to a 2D Model

The 3D model presented here is different to the earlier 2D model [44], and here we will highlight three of the main differences.

First, microtubule collision is different in 3D compared to 2D, as two infinite non-parallel lines will always intersect in 2D but not in 3D, so in 3D microtubule thickness plays a more important role in determining the conditions for a potential phase transition. Mathematically, this causes the induced catastrophe flux term (Eq. 5) to be different in 2D and 3D. In 3D, a new factor of d_m is necessary for dimensional agreement and for the effect of microtubule thickness on collision probability to be reflected in the flux term. Additionally, the factor $|\sin(\sigma)|$ which adjusts for varying collision probability on angle has a different angular dependence with the collision angle defined in 3D (Eq. 7) as $\sigma = \arccos(\sin(\theta)\sin(\theta')\cos(\phi - \phi') + \cos(\theta)\cos(\theta'))$ instead of $\sigma = (\phi - \phi')$ in 2D [44] with ϕ defined as the 2D polar angle in the usual way.

Second, a technical difference is the role that spherical harmonic modes have taken in this 3D mean-field theory, replacing a similar role played by Fourier modes in 2D. The change is caused by the factor of $|\sin(\sigma)|$ in the catastrophe flux term, which significantly changes the calculation in Sec. II A 4, and leads to a different linear operator defined in Eq. 8. In 3D, the spherical harmonics provide an orthonormal basis of eigenfunctions, instead of Fourier modes in 2D. Viewing the spherical harmonics $Y_\ell^m : S^2 \rightarrow \mathbb{R}$ as a higher dimensional analog of $S^1 \rightarrow \mathbb{R}$ Fourier modes [53], this higher dimensional generalization is not unexpected. As a result of this difference, Eq. 27 and Eq. 28 both involve Legendre coefficients in 3D instead of Fourier coefficients in 2D.

Third, the predicted value of G for which a phase transition is possible takes a different form in 3D compared to 2D, although there are subtle similarities. Specifically, $G \propto l_0$ and in 3D l_0 itself is a fourth root (Eq. 12), so taking the negative solution for l_0 results in positive $G = gl_0$ when g is negative, which is a requirement for bounded growth. The non-dimensional control parameter G has a different form in 3D and 2D, despite the dimensional control parameter $g = r_c/v^- - r_r/v^+$ remaining the same. This arises as there are expected differences in the definition of l_0 , necessary to ensure it has dimensions of length. There are also differences in the factors of l_0 involved in non-dimensionalizing g (to G) and other vari-

ables describing the system. The control parameter can be modified by multiplying by any dimensionless function without fundamentally changing the system, but the expression for the critical value must be correspondingly updated. Since a dimensionless factor of $\alpha^{1/3}$ enters the expression for the critical value of G (Eq. 37) at which a phase transition is possible, we define an effective control parameter $G_{\text{eff}} \equiv G\alpha^{-1/3} = gl_0^{4/3}d_m^{-1/3}$. Written in this form, this 3D effective control parameter is proportional to the 2D control parameter in [44] multiplied by a factor of $d_m^{-1/3}$. Since our prediction for G_{eff} is a purely numeric quantity, since the critical value $G^* \equiv 1.56\alpha^{1/3}$ is now equivalent to $G_{\text{eff}}^* = 1.56$, this will be used when we compare to simulation in the next section. G_{eff} can be written explicitly as

$$G_{\text{eff}} = \left[\frac{4\pi v^+ v^-}{r_n(v^+ + v^-)} \right]^{\frac{1}{3}} \left(\frac{r_r}{v^-} - \frac{r_c}{v^+} \right) d_m^{-\frac{1}{3}}. \quad (43)$$

C. Comparison to Simulation

Next, we compare our mean-field theory predictions against computational simulations (described in Sec. II B). Specifically, we test three mean-field theory predictions: decreasing G_{eff} causes an increase in anisotropy; a phase transition is only possible at approximately $G_{\text{eff}}^* = 1.56$ (3sf); and the zippering probability function does not affect the other two predictions.

From Eq. 43, $G_{\text{eff}} \propto r_n^{-1/3}$ and $G_{\text{eff}} \propto r_c$ so to vary G_{eff} in simulations, we directly vary r_n and r_c . We make a specific choice of r_n and r_c to keep the average steady state number of microtubule segments within a fixed range in the volume within which we perform our anisotropy calculation (Fig. 6). This is to remove any effect of microtubule density on the anisotropy levels of the system. Using a dimensional argument, we can determine the relationship between r_c and r_n required to keep the microtubule density constant. Microtubule lifetime is proportional to $1/r_c$ (this is more clear in the case without rescue), resulting in a mean microtubule length proportional to v^+/r_c . The number of microtubules is proportional to r_n/r_c for similar reasons. Therefore, imposing that the total density of microtubule segments be constant is equivalent to the condition that $v^+/r_c \times r_n/r_c$ be constant. This suggests that when v^+ is kept constant, $r_n \propto r_c^2$ ensures a constant density of microtubule segments. We corroborated this prediction in simulations within a $r_n - r_c$ region where density fluctuations (after converging to a steady state density) were small and convergence occurred within reasonable computation times (Fig. 6). The $r_n - r_c$ path of constant microtubule density of 100,000 segments forms a curve, to which statistically fitting a power law indicates it is approximately a quadratic. To go from the case of 100,000 segments to 200,000 segments, r_n is approximately doubled for each r_c (Fig. 6), but statistical fitting indicates it is still approx-

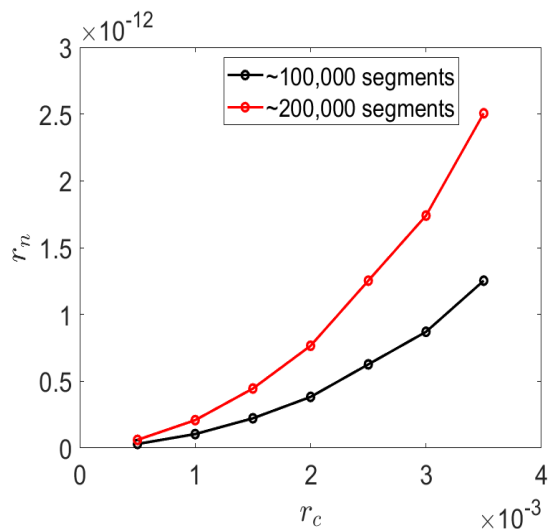


FIG. 6: Paths in the $r_n - r_c$ plane which give constant microtubule segment numbers of $100,000 \pm 5,000$ (blue) and $200,000 \pm 10,000$ (red), averaged over 50 simulations for each point in parameter space.

imately a quadratic, matching our theoretical estimate.

We then investigated how the directional anisotropy changed with varying G_{eff} . The mean-field theory prediction that increasing G_{eff} corresponds to decreasing levels of anisotropy (estimated by S), indicating a change from a more ordered to less ordered state is confirmed in the simulations (Fig. 7). Furthermore, the G_{eff} region for which we are observing this decrease in microtubule order supports the prediction of $G_{\text{eff}}^* = 1.56$ as an order of magnitude estimate for a change from an isotropic to anisotropic system.

Next, we investigated the effect of zippering on the change in anisotropy for varying G_{eff} . The similar behavior with and without zippering verifies the prediction that changing $P_z(\sigma)$ has no effect on the orientational dynamics of the system (Fig. 7). Comparing the simulations at the lowest and highest values of G_{eff} in Fig. 7 for the zippering and no-zippering case we observe a statistically significant decrease in anisotropy in both cases (using a 2-sample Kolmogorov-Smirnoff test, p-values 1.1×10^{-3} and 3.5×10^{-7} respectively). This is despite non-trivial differences in anisotropy at each G_{eff} between simulations (Appendix C specifically Fig. A1). Therefore, our simulations have verified that zippering does not effect the order of the microtubule system and both zippering setups show the theoretically predicted statistically significant decrease in anisotropy with increasing G_{eff} .

D. Effect of Severing

Both through mean-field theory and simulations, we have shown that crossover severing is not necessary for the anisotropy level of our system to increase as we decrease

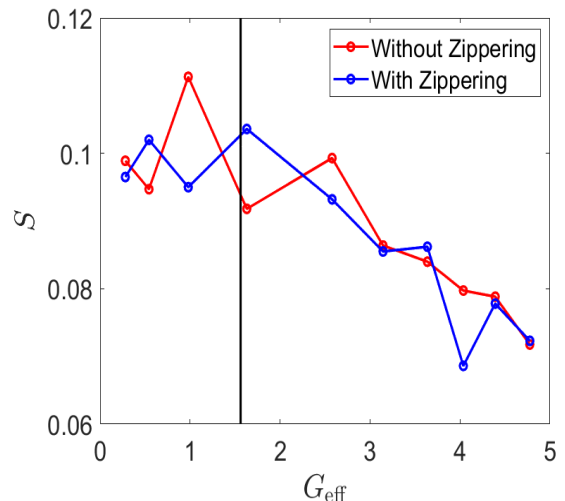


FIG. 7: Anisotropy S , plotted against increasing effective control parameter G_{eff} with zippering (blue) and without zippering (red). The black line marks the mean-field theory prediction of the only place a phase transition can occur at $G_{\text{eff}}^* = 1.56$.

the control parameter G_{eff} . Introducing the effects of severing into the mean-field theory framework is beyond the scope of this paper, however it is straightforward to incorporate severing into the simulations to see how it affects the dynamics of the system.

Incorporating severing in simulations led to a greater change in anisotropy for the same change in G_{eff} when compared to the no-severing case, as demonstrated by the steeper gradient in Fig. 8. However, the inclusion of severing more commonly reduced the microtubule density, but also increased the variation in segment number with the segment densities now varying significantly between 27,000 and 78,000. It is expected that segment density would impact the system anisotropy. Therefore, we compensate by doubling r_n so that the segment densities remain within the same range as those of the no-severing simulation. We still observe increasing G_{eff} causes a decrease in S but anisotropy matches the results from simulations without severing more closely, as shown in Fig. 8.

We conclude that the mean-field theory prediction of anisotropy increasing for decreasing G_{eff} is robust to the inclusion of severing. Furthermore, the higher variation in anisotropy with varying G_{eff} seems to result from the effect severing has on microtubule segment density. When this effect is adjusted for, we get similar quantitative behavior in the simulation results with or without severing included.

E. Comparison to Experiment

Properties of microtubules have been experimentally measured in different systems, with some examples from the literature shown in Table. I. From these values we

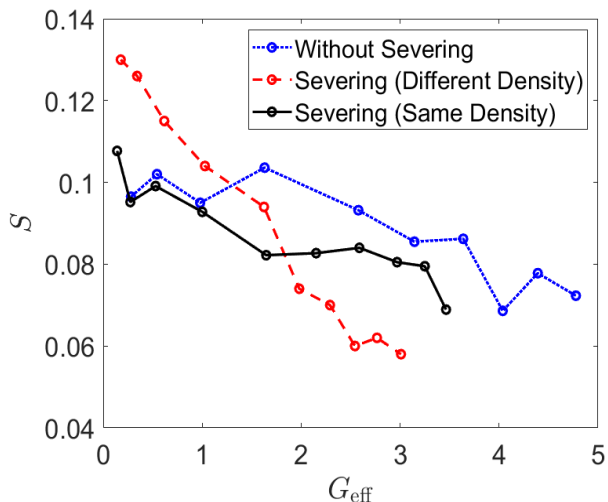


FIG. 8: Simulation results, similar to Fig. 7, showing the effect of severing on anisotropy as the control parameter G_{eff} is increased. The case without severing (blue) is repeated from Fig. 7 for comparison. Simulation results with severing included and r_n doubled are plotted (green) as well as simulation results with severing included and the segment density kept at approximately $50,000 \pm 5,000$ through changing r_n (red).

can calculate G_{eff} using Eq. 43). For example, for tobacco interphase microtubules [54], we obtain

$$\begin{aligned}
 G_{\text{eff}} &= \left(\frac{4\pi \times 18.36 \mu\text{m}/\text{min} \times 4.59 \mu\text{m}/\text{min}}{18.36 \mu\text{m}/\text{min} + 4.59 \mu\text{m}/\text{min}} \right)^{1/3} \\
 &\times \left(\frac{60 \times 0.015/\text{min}}{18.36 \mu\text{m}/\text{min}} - \frac{60 \times 0.051/\text{min}}{4.59 \mu\text{m}/\text{min}} \right) \quad (44) \\
 &\times (0.024 \mu\text{m})^{-1/3} \times (r_n)^{-1/3} \\
 &= -7.7(r_n)^{-1/3}.
 \end{aligned}$$

Here, the negative value of g corresponds to bounded (and therefore physically realistic) growth in the mean-field theory model. Using our mean-field theory predicted value of $G_{\text{eff}}^* = 1.56$ gives us an order of magnitude estimate for the nucleation rate at which anisotropy enters the system of $r_n \approx 120/\mu\text{m}^3/\text{min}$. A similar calculation for the other microtubule systems in Table. I gives values ranging over four orders of magnitude from 0.7 – 1040. This compares to the magnitude of microtubule nucleation rates used in simulations for microtubules restricted to 2D surfaces of $0.06/\mu\text{m}^2/\text{min}$ [27] and $0.02/\mu\text{m}^2/\text{min}$ [55]. As these nucleation rates are low compared to those calculated for the onset of order in Table. I, this suggests larger nucleation rates are required in 3D compared to 2D for order in the microtubule system. We have found few experimental studies which report nucleation rates per unit area (or volume) per time. However, we can estimate a surface nucleation rate r_n from the measured number of nucleations and centrosome size in [56] which

Source	v^+	v^-	r_r	r_c	r_n prediction
Tobacco Interphase [54]	4.59	18.36	0.051	0.015	120
Tobacco Preprophase [54]	6.88	17.89	0.065	0.029	71
Xenopus IgG injected [57]	4.8	6.4	0.0203	0.0116	1.2
Xenopus Anti-XKCM1 [57]	4	10	0.0378	0.0056	60
Suspension in vitro [58]	1.9	9.7	≈ 0.005 estimate	≈ 0.002 estimate	0.7
Chinese hamster ovary (leading) [59]	11	14	0.2	0.005	1040

TABLE I: Experimental values from the literature for microtubule growth conditions and the value we predict for each system of r_n for anisotropy entering the system from our MFT calculation. Growth speeds are stated in units of $\mu\text{m}/\text{min}$, catastrophe and rescue rates in units of $/\text{s}$ and r_n in $/\mu\text{m}^3/\text{min}$. Estimates of catastrophe and rescue rates from [58] are obtained by modelling MTs as Bernoulli trials, assuming a 0.5 chance of rescue after two shrink events and an average of 10 growth events before a catastrophe to reach $20\mu\text{m}$ reported average length.

gives $r_n \approx 40/\mu\text{m}^2/\text{min}$. Although, per area rather than per volume, this magnitude is within the (per volume) ranges we see in Table. I.

IV. DISCUSSION AND OUTLOOK

In this work, we have developed a 3D mean-field theory model for an interacting system of microtubules. Having established an isotropic solution to this model, we showed that a perturbative solution and therefore a phase transition can only occur for one value of the effective control parameter $G_{\text{eff}}^* = 1.56$ (3sf). The existence of G_{eff}^* was established analytically and its value was numerically calculated with input from experimental estimates for collision event probabilities. We then utilized simulations to verify that anisotropy increased for decreasing G_{eff} , and the region we observe this decrease coincides with the mean-field theory prediction for the phase transition $G_{\text{eff}}^* = 1.56$ suggesting is a reasonable order of magnitude estimate for anisotropy entering the system.

The mean-field theory model furthermore predicts that the critical value G_{eff}^* only depends on the induced catastrophe probability function, not the zippering probability function, with our simulations verifying that zippering did not affect the anisotropy dependence on G_{eff}^* . In simulations, cross-over severing similarly did not effect the decrease in anisotropy with increasing G_{eff} provided microtubule density was accounted for, but incorporating this in the mean-field theory model was beyond the scope of this paper.

There are several ways in which the novel 3D mean-field theory model introduced in this paper could be developed further. Firstly, the effects of crossover severing [15] could be included within the framework of mean-field theory. This may be possible by altering the length density function by weighting towards shorter microtubule lengths, constrained by the conservation of microtubule length upon splitting. Secondly, a hard boundary could be introduced to the mean-field theory model to allow the study of different cell geometries, although the exact formulation to achieve this is currently unclear. Thirdly, solving the full non-perturbative steady state equations Eqs. 15 and studying their solution, would lead to a better understanding of the phase transition taking place. Mean-field theory is an interesting mathematical framework to further explore and analyze microtubules in contrast to computationally intensive simulations and experiments and is a step to bridge scales from analyzing local microtubule behaviors to multicellular simulations.

Acknowledgments All three authors acknowledge support from the Gatsby Charitable Foundation (GAT3395/PR4B) and additionally T.A.S and H.J acknowledge support from the Human Frontier Science Program Organization (Grant RGP0009/2018). We thank François Nédélec and Bø Sodeberg for useful discussions in relation to formulating the mean-field theory, as well as Ross Carter for assistance with computational issues.

Data availability The 3D microtubule simulations were run using Tubulaton.

<https://gitlab.com/slucu/teamHJ/tubulaton>.

Details of how to reproduce figures in this paper are available here along with matlab analysis scripts

https://gitlab.com/slucu/teamHJ/publications/gibson_et_al_2022.

Appendix A: Relating isotropic variables to \mathbf{G}

Here, proofs of Eq. 28 and Eq. 31 are given.

Eq. 27d can be rewritten in the form

$$\bar{R} = \frac{\bar{L}}{1 - 4\pi\alpha\mathfrak{Z}_0\bar{L}\bar{K}}. \quad (\text{A1})$$

Eq. 27c can also be rewritten as

$$1 + \bar{Q} = \frac{1}{1 - 4\pi\alpha\mathfrak{Z}_0\bar{L}\bar{K}}. \quad (\text{A2})$$

Substituting this expression for $1 + \bar{Q}$ into Eq. 27b results in

$$\bar{K} = \frac{\bar{L}^2}{(1 - 4\pi\alpha\mathfrak{Z}_0\bar{L}\bar{K})^2}. \quad (\text{A3})$$

Comparing Eq. A1 and Eq. A3 leads to the relation

$$\bar{K} = \bar{R}^2. \quad (\text{A4})$$

\bar{T} from Eq. 27d can be substituted into the reciprocal of this identity to obtain

$$\frac{1}{\bar{K}} = \frac{1}{\bar{R}^2} = \left(\frac{1}{\bar{L}} - 4\pi\alpha\mathfrak{Z}_0\bar{K} \right)^2. \quad (\text{A5})$$

Substituting for the expression in parentheses using Eq. 27a leads to

$$\frac{1}{\bar{K}} = (4\pi\alpha\mathfrak{C}_0\bar{K} - G)^2. \quad (\text{A6})$$

Thus, an expression equivalent to Eq. 28 is obtained. Eq. A3 can be rewritten as

$$\bar{N}(1 - 4\pi\alpha\mathfrak{Z}_0\bar{N})^2 = \bar{L}^3. \quad (\text{A7})$$

Eq. 27a can also be rewritten

$$\bar{L} = \frac{(4\pi\alpha(\mathfrak{Z}_0 + \mathfrak{C}_0)\bar{N} - 1)^2}{G}. \quad (\text{A8})$$

Substituting this expression for \bar{L} into Eq. A7 and rearranging for G^3 leads to

$$G^3 = \frac{(4\pi\alpha(\mathfrak{Z}_0 + \mathfrak{C}_0)\bar{N} - 1)^3}{\bar{N}(1 - 4\pi\alpha\mathfrak{Z}_0\bar{N})^2}. \quad (\text{A9})$$

This is equivalent to Eq. 31.

Appendix B: Eigenvalue equation for first order perturbations

Here, a proof of Eq. 37 is provided. Small perturbations $\lambda(\theta, \phi), \kappa(\theta, \phi), \chi(\theta, \phi), \rho(\theta, \phi)$ to the steady state isotropic system are defined with

$$\begin{aligned} L &= \bar{L}(1 + \lambda), \\ K &= \bar{K}(1 + \kappa), \\ Q &= \bar{Q}(1 + \chi), \\ R &= \bar{R}(1 + \rho). \end{aligned} \quad (\text{B1})$$

Inserting Eqs. B1 into Eq. 15b leads to

$$\bar{K} + \bar{K}\kappa = (\bar{L} + \bar{L}\lambda)(\bar{R} + \bar{R}\rho)(1 + \bar{Q} + \bar{Q}\chi). \quad (\text{B2})$$

Substituting for $(1 + \bar{Q})$ from Eq. 27b leads to

$$\bar{K} + \bar{K}\kappa = (\bar{L}\bar{R} + \bar{L}\bar{R}(\lambda + \rho) + \mathcal{O}(\lambda\rho)) \left(\frac{\bar{K}}{\bar{L}\bar{R}} + \bar{Q}\chi \right). \quad (\text{B3})$$

Disregarding second (and higher) order terms, this rearranges to

$$\kappa = \lambda + \rho + \left(\frac{\bar{Q}}{\bar{K}} \bar{L}\bar{R}\chi \right). \quad (\text{B4})$$

Substituting for \bar{Q}/\bar{K} from Eq. 27c divided by Eq. 27b results in

$$\kappa = \lambda + \rho + 4\pi\alpha\mathfrak{Z}_0\bar{L}\bar{K}\chi. \quad (\text{B5})$$

This directly implies that

$$Z[\kappa] = Z[\lambda + \rho + 4\pi\alpha\mathfrak{Z}_0\bar{L}\bar{K}\chi]. \quad (\text{B6})$$

Inserting Eqs. B1 into 15c and disregarding second order terms gives

$$\bar{Q} + \bar{Q}\chi = \bar{L}\bar{K}(1 + \bar{Q})Z[1 + \lambda + \kappa + \chi] + \bar{L}\bar{K}\bar{Q}Z[\chi]. \quad (\text{B7})$$

Subtracting Eq. 27c and dividing through by \bar{Q} leaves

$$\chi = \bar{L}\bar{K} \left(\frac{1 + \bar{Q}}{\bar{Q}} \right) Z[\lambda + \kappa] + \bar{L}\bar{K}Z[\chi]. \quad (\text{B8})$$

Substituting for $(1 + \bar{Q})/\bar{Q}$ from Eq. 27c gives

$$\chi = \frac{1}{4\pi\alpha\mathfrak{Z}_0} Z[\lambda + \kappa + 4\pi\alpha\mathfrak{Z}_0\bar{L}\bar{K}\chi]. \quad (\text{B9})$$

Inserting Eqs. B1 into Eq. 15d and subtracting Eq. 27d gives

$$\rho = \left(\frac{\bar{L}}{\bar{R}} \right) \lambda + 4\pi\alpha\mathfrak{Z}_0\bar{L}\bar{K}(\lambda + \kappa) + \bar{L}\bar{K}Z[\rho]. \quad (\text{B10})$$

Using Eq. 27d again to rewrite the coefficient of λ leads to

$$\rho = \lambda + \bar{L}\bar{K}(4\pi\alpha\mathfrak{Z}_0\kappa + Z[\rho]). \quad (\text{B11})$$

From B6,B9,B11 the following expression for $Z[\kappa]$ can be obtained

$$Z[\kappa] = \frac{1}{2} \left(\frac{\rho - \lambda}{\bar{L}\bar{K}} + 4\pi\alpha\mathfrak{Z}_0(\chi - \kappa) \right). \quad (\text{B12})$$

Inserting Eqs. B1 into Eq. 15a, subtracting Eq. 27a and taking the first order approximation $(1 + \lambda)^{-1} \approx 1 - \lambda$ results in

$$\lambda = -\bar{L}\bar{K}(C[\kappa] + Z[\kappa]). \quad (\text{B13})$$

Eq. B12 can be substituted into B13 to obtain

$$2\lambda = -2\bar{L}\bar{K}C[\kappa] - \rho + \lambda - 4\pi\alpha\mathfrak{Z}_0\bar{L}\bar{K}\chi + 4\pi\alpha\mathfrak{Z}_0\bar{L}\bar{K}\kappa. \quad (\text{B14})$$

Finally, substituting κ for the expression in Eq. B5 leads to

$$-2\bar{L}\bar{K}C[\kappa] = (1 - 4\pi\alpha\mathfrak{Z}_0\bar{L}\bar{K})\kappa. \quad (\text{B15})$$

Appendix C: Variation and convergence of simulations

Fig. A1 shows (with boxplots) the variation of Anisotropy at increasing G_{eff} from 50 simulations at each parameter pair with and without zippering. Furthermore, for $G_{\text{eff}} = 3.1$, we plot the segment density against time for 10 simulations. This justifies our assumption that the density of the system converges to a steady state subject to small fluctuations. For higher G_{eff} , the speed of convergence is quicker and similarly slower at lower G . To further verify that we reach a steady state within 10,000 timesteps, we observed that the average steady state density stayed within $50,000 \pm 3,000$ when the time was extended to 30,000 time steps.

Appendix D: Simulation Parameter Values

Default parameter values used for the Tubulaton simulations are listed here in Table. A2.

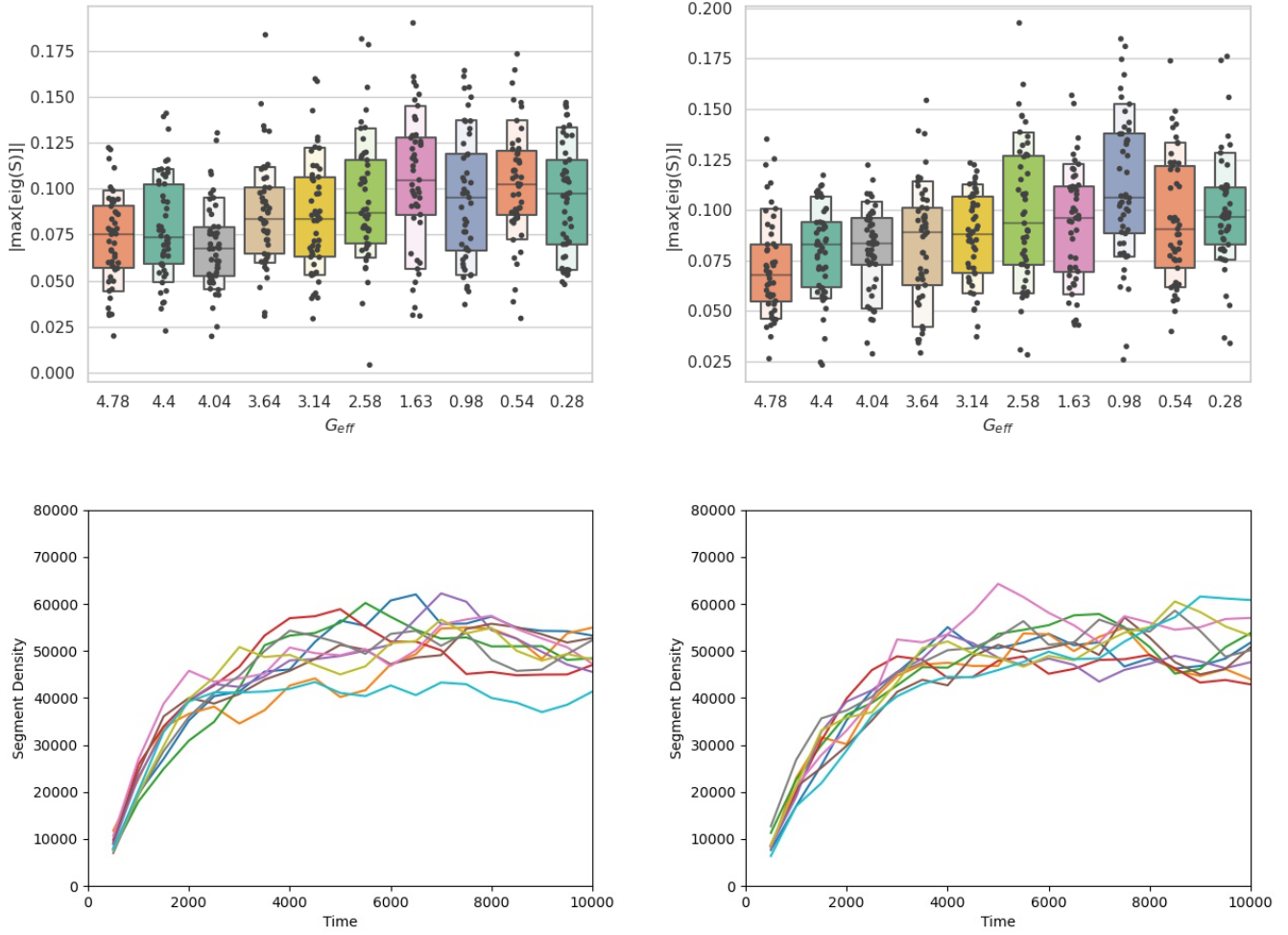


FIG. A1: Simulation results with zippering (left) and without zippering (right) and without severing in all cases. (Top) Boxplots showing variation in maximum eigenvalue across all 50 simulation results for each parameter pair. (Bottom) Change in number of microtubule segments over the first 10,000 timesteps for each of 10 different simulations at $G_{\text{eff}} = 3.1$.

Parameter	Value
Zippering Angle	0.7 radians
Boundary zippering angle threshold	0.7 radians
Interaction distance	49 nm
Probability of induced catastrophe	$P_c(\sigma) = \sigma/2 \quad \forall \sigma \leq \pi/2$ and $P_c(\sigma) = \pi/2 - \sigma/2$ o/w
Probability of Zippering	$P_z(\sigma) = 1 - P_c(\sigma) \quad \forall \sigma \leq 0.7, \sigma \geq \pi - 0.7$ and $P_z(\sigma) = 0$ o/w
Probability of spontaneous catastrophe	$(0.06-3.5) \times 10^{-3}$
Probability of cutting crossing microtubule	0.005
Random microtubule shrinkage from plus-end	0
Probability of detachment	0.0005 per nucleation site per time step
Nucleation rate	$(0.145-5.8) \times 10^{-1}$
Initial nucleations	0
Minus/Plus end shrink/growth speed respectively	$0.08-0.04 \mu\text{s}^{-1}$
Boundary sphere radius	10,000 or 1000 units (80 or 8 μm)
Nucleation sphere radius (R_1)	7,000 or 700 units (56 or 5.6 μm)
Analysis sphere radius	4,000 or 500 units (32 or 4 μm)
Number of time steps	10,000
Number of repeats	50

TABLE A2: List of default parameters for the Tubulaton simulations.

- [1] R. Wade. On and around microtubules: An overview. *Mol. Biotechnol.*, 43:177–91, 2009.
- [2] B. B. Buchanan, W. Gruissem, and R. L. Jones. *Biochemistry and Molecular Biology of Plants*. Wiley, 2015.
- [3] C. G. Rasmussen, A. J. Wright, and S. Müller. The role of the cytoskeleton and associated proteins in determination of the plant cell division plane. *Plant J.*, 75(2):258–269, 2013.
- [4] L. Bashline, L. Lei, S. Li, and Y. Gu. Cell wall, cytoskeleton, and cell expansion in higher plants. *Mol. Plant*, 7(4):586–600, 2014.
- [5] W. E. Hable, S. R. Bisgrove, and D. L. Kropf. To Shape a Plant—The Cytoskeleton in Plant Morphogenesis. *Plant Cell*, 10(11):1772–1774, 1998.
- [6] A. Geitmann and A. Nebenführ. Navigating the plant cell: intracellular transport logistics in the green kingdom. *Mol. Biol. Cell*, 26(19):3373–3378, 2015.
- [7] M. Bringmann, B. Landrein, C. Schudoma, O. Hamant, M-T. Hauser, and S. Persson. Cracking the elusive alignment hypothesis: the microtubule–cellulose synthase nexus unraveled. *Trends Plant Sci.*, 17:666 – 674, 2012.
- [8] S. Reinsch and P. Gonczy. Mechanisms of nuclear positioning. *J. Cell Sci.*, 111(16):2283–2295, 1998.
- [9] G. Schatten, C. Simerly, and H. Schatten. Microtubule configurations during fertilization, mitosis, and early development in the mouse and the requirement for egg microtubule-mediated motility during mammalian fertilization. *Proc. Natl. Acad. Sci. U.S.A.*, 82:4152–6, 1985.
- [10] R. H. Goddard, S. M. Wick, C. D. Silflow, and D. P. Snustad. Microtubule Components of the Plant Cell Cytoskeleton. *Plant Physiol.*, 104(1):1–6, 1994.
- [11] D. A. Fletcher and R. D. Mullins. Cell mechanics and the cytoskeleton. *Nature*, 463:485–492, 2010.
- [12] G. J. Brouhard. Dynamic instability 30 years later: complexities in microtubule growth and catastrophe. *Mol. Biol. Cell*, 26(7):1207–1210, 2015.
- [13] R. Dixit and R. Cyr. Encounters between Dynamic Cortical Microtubules Promote Ordering of the Cortical Array through Angle-Dependent Modifications of Microtubule Behavior[W]. *Plant Cell*, 16(12):3274–3284, 2004.
- [14] C. J. Ambrose and G. O. Wasteneys. Clasp modulates microtubule-cortex interaction during self-organization of acentrosomal microtubules. *Mol. Biol. Cell*, 19(11):4730–4737, 2008.
- [15] A. Roll-Mecak and F. J. McNally. Microtubule-severing enzymes. *Curr. Opin. Cell Biol.*, 22(1):96–103, 2010. Cell structure and dynamics.
- [16] M. Piehl, U. S. Tulu, P. Wadsworth, and L. Cassimeris. Centrosome maturation: Measurement of microtubule nucleation throughout the cell cycle by using gfp-tagged eb1. *Proc. Natl. Acad. Sci. U.S.A.*, 101(6):1584–1588, 2004.
- [17] Y. Oda. Cortical microtubule rearrangements and cell wall patterning. *Front. Plant Sci.*, 6, 2015.
- [18] M. Yamada and K. Hayashi. Microtubule nucleation in the cytoplasm of developing cortical neurons and its regulation by brain-derived neurotrophic factor. *Cytoskeleton*, 76(5):339–345, 2019.
- [19] Y. Nakaoka, A. Kimura, T. Tani, and G. Goshima. Cytoplasmic Nucleation and Atypical Branching Nucleation Generate Endoplasmic Microtubules in *Physcomitrella patens*. *Plant Cell*, 27(1):228–242, 2015.
- [20] P. G. De Gennes and J. Prost. *The Physics of Liquid Crystal*, volume 2. Oxford University Press, 1993.
- [21] D. Andrienko. Introduction to liquid crystals. *J. Mol. Liq.*, 267:520–541, 2018.
- [22] A. L. Hitt, A. R. Cross, and R. C. Williams. Microtubule solutions display nematic liquid crystalline structure. *J. Biol. Chem.*, 265 3:1639–47, 1990.
- [23] M. C. Lagomarsino, C. Tanase, J. W. Vos, A. M. C. Emons, B. M. Mulder, and M. Dogterom. Microtubule organization in three-dimensional confined geometries: Evaluating the role of elasticity through a combined in vitro and modeling approach. *Biophys. J.*, 92(3):1046–1057, 2007.
- [24] E. C. Eren, R. Dixit, and N. Gautam. A three-dimensional computer simulation model reveals the mechanisms for self-organization of plant cortical microtubules into oblique arrays. *Mol. Biol. Cell*, 21(15):2674–2684, 2010.
- [25] V. A. Baulin, C. M. Marques, and F. Thalmann. Collision induced spatial organization of microtubules. *Biophys. Chem.*, 128(2):231–244, 2007.
- [26] Corticalsim. <https://github.com/corticalsim/corticalsim>. Accessed: September 2022.
- [27] S. Tindemans, E. Deinum, J. Lindeboom, and B. M. Mulder. Efficient event-driven simulations shed new light on microtubule organization in the plant cortical array. *Front. Phys.*, 2, 2014.
- [28] E. E. Deinum, S. H. Tindemans, and B. M. Mulder. Taking directions: the role of microtubule-bound nucleation in the self-organization of the plant cortical array. *Phys. Biol.*, 8(5):056002, 2011.
- [29] Cytosim. <https://gitlab.com/f-nedelec/cytosim>. Accessed: September 2022.
- [30] B. Rupp and F. Nédélec. Patterns of molecular motors that guide and sort filaments. *Lab Chip*, 12:4903–4910, 2012.
- [31] Tubulaton. <https://gitlab.com/slcu/teamHJ/tubulaton>.
- [32] V. Mirabet, P. Krupinski, O. Hamant, E. M. Meyerowitz, H. Jönsson, and A. Boudaoud. The self-organization of plant microtubules inside the cell volume yields their cortical localization, stable alignment, and sensitivity to external cues. *PLOS Comput. Biol.*, 14:e1006011, 2018.
- [33] P. Durand-Smet, T. A. Spelman, E. M. Meyerowitz, and H. Jönsson. Cytoskeletal organization in isolated plant cells under geometry control. *Proceedings of the National Academy of Sciences*, 117(29):17399–17408, 2020.
- [34] E. Geigant, K. Ladizhansky, and A. Mogilner. An integro-differential model for orientational distributions of f-actin in cells. *SIAM J. Appl. Math.*, 59:787–809, 1997.
- [35] I. S. Aranson and L. S. Tsimring. Theory of self-assembly of microtubules and motors. *Phys. Rev. E*, 74:031915, 2006.
- [36] V. Rühle, F. Ziebert, R. Peter, and W. Zimmermann. Instabilities in a two-dimensional polar-filament-motor system. *Eur. Phys. J. E*, 27:243–51, 2008.
- [37] S. Yarahmadian and M. Yari. Phase transition analysis of the dynamic instability of microtubules. *Nonlinearity*, 27, 2013.

- [38] S. K. Ma. *Modern theory of critical phenomena*. Routledge, 2018.
- [39] M. Dogterom and S. Leibler. Physical aspects of the growth and regulation of microtubule structures. *Phys. Rev. Lett.*, 70:1347–1350, 1993.
- [40] P. M. Chaikin and T. C. Lubensky. *Mean-field theory*, page 144–212. Cambridge University Press, 1995.
- [41] A. R. Lamson, J. M. Moore, F. Fang, M. A. Glaser, M. J. Shelley, and M. D. Betterton. Comparison of explicit and mean-field models of cytoskeletal filaments with crosslinking motors. *Eur. Phys. J. E*, 44:1–22, 2021.
- [42] X. Q. Shi and Y. Q. Ma. Understanding phase behavior of plant cell cortex microtubule organization. *Proc. Natl. Acad. Sci. U.S.A.*, 107(26):11709–11714, 2010.
- [43] V. A. Baulin, C. M. Marques, and F. Thalmann. Collision induced spatial organization of microtubules. *Biophys. Chem.*, 128(2):231–244, 2007.
- [44] R. J. Hawkins, S. H. Tindemans, and B. M. Mulder. Model for the orientational ordering of the plant microtubule cortical array. *Phys. Rev. E*, 82:011911, 2010.
- [45] P. Foteinopoulos. *Models for spatial organization of microtubules and cell polarization*. PhD thesis, Wageningen University, 2019.
- [46] N. M. Ferrers. *An Elementary Treatise on Spherical Harmonics and Subjects Connected with Them*. Macmillan and Co., London, 1877.
- [47] K. Atkinson and W. Han. *Spherical Harmonics and Approximations on the Unit Sphere: An Introduction*. Lecture Notes in Mathematics. Springer Berlin Heidelberg, Berlin, Heidelberg, 2012 edition, 2012.
- [48] X. Lamy. Uniaxial symmetry in nematic liquid crystals. *Ann. I. H. Poincaré-AN*, 32(5):1125–1144, 2015.
- [49] H. Löwen. Anisotropic self-diffusion in colloidal nematic phases. *Phys. Rev. E*, 59:1989–1995, 1999.
- [50] H. Wang. A new and sharper bound for legendre expansion of differentiable functions. *Appl. Math. Lett.*, 85:95–102, 2018.
- [51] V. A. Antonov and K. V. Holvevnikov. An estimate of the remainder in the expansion of the generating function for the legendre polynomials (generalization and improvement of bernstein’s inequality). *Vestn. St. Petersburg Univ.: Math.*, 13:163–166, 1981.
- [52] L. Lorch. Alternative proof of a sharpened form of bernstein’s inequality for legendre polynomials. *Appl. Anal.*, 14(3):237–240, 1983.
- [53] H. Kalf. On the expansion of a function in terms of spherical harmonics in arbitrary dimensions. *Bull. Belg. Math. Soc. Simon Stevin*, 2(4):361 – 380, 1995.
- [54] P. Dhonukshe and T. W. J. Gadella. Alteration of Microtubule Dynamic Instability during Preprophase Band Formation Revealed by Yellow Fluorescent Protein–CLIP170 Microtubule Plus-End Labeling[W]. *Plant Cell*, 15(3):597–611, 2003.
- [55] Y. Nakaoka, A. Kimura, T. Tani, and G. Goshima. Cytoplasmic nucleation and atypical branching nucleation generate endoplasmic microtubules in *Physcomitrella patens*. *Plant Cell*, 27(1):228–242, 2015.
- [56] M. Piehl, U. S. Tulu, P. Wadsworth, and L. Cassimeris. Centrosome maturation: Measurement of microtubule nucleation throughout the cell cycle by using gfp-tagged eb1. *Proc. Natl. Acad. Sci. U.S.A.*, 101(6):1584–1588, 2004.
- [57] S. L. Kline-Smith and C. E. Walczak. The microtubule-destabilizing kinesin *xkcm1* regulates microtubule dynamic instability in cells. *J. Mol. Cell Biol.*, 13(8):2718–31, 2002.
- [58] T. Mitchison and M. Kirschner. Dynamic instability of microtubule growth. *Nature*, 312:237–242, 1984.
- [59] K. J. Salaycik, C. J. Fagerstrom, K. Murthy, U. S. Tulu, and P. Wadsworth. Quantification of microtubule nucleation, growth and dynamics in wound-edge cells. *J. Cell Sci.*, 118(18):4113–4122, 2005.